

# Discovery and properties of ultra-high redshift galaxies ( $9 < z < 12$ ) in the JWST ERO SMACS 0723 Field

N.J. Adams<sup>1\*</sup>, C.J. Conselice,<sup>1</sup> L. Ferreira,<sup>2</sup> D. Austin,<sup>1</sup> J. Trussler,<sup>1</sup> I. Juodžbalis,<sup>1</sup> S. M. Wilkins,<sup>3,4</sup> J. Caruana,<sup>4,5</sup>, P. Dayal<sup>6</sup>

<sup>1</sup>Jodrell Bank Centre for Astrophysics, University of Manchester, Oxford Road, Manchester, UK

<sup>2</sup>Department of Physics and Astronomy, University of Nottingham, NG7 2RD, UK

<sup>3</sup>Astronomy Centre, University of Sussex, Falmer, Brighton BN1 9QH, UK

<sup>4</sup>Institute of Space Sciences & Astronomy, University of Malta, Msida MSD 2080, Malta

<sup>5</sup>Department of Physics, University of Malta, Msida MSD 2080, Malta

<sup>6</sup>Kapteyn Astronomical Institute, University of Groningen, P.O. Box 800, 9700 AV Groningen, The Netherlands

Accepted XXX. Received YYY; in original form ZZZ

## ABSTRACT

We present a reduction and analysis of the *James Webb Space Telescope* (JWST) SMACS 0723 field to conduct a search for ultra-high-redshift galaxies ( $9 < z < 12$ ) present within the Epoch of Reionization. We use a combination of photometric redshifts and spectral energy distribution (SED) modelling-based selection criteria to optimise sample completeness while minimising contamination. We find four  $z > 9$  candidate galaxies which have not previously been identified, with one object at  $z = 11.5$ , and another which is possibly a close pair of galaxies. These sources are fairly bright with  $m_{277} \sim 26 - 28$ . A significant fraction of these sources show evidence for Balmer-breaks or extreme emission lines from H $\beta$  and [OIII], demonstrating that the stellar populations could be quite advanced in age or very young depending on the exact cause of the F444W excess. We discuss the stellar masses and resolved structures of these early galaxies and find that the Sérsic indices reveal a mixture of light concentration levels, but that the sizes of all our systems are exceptionally small in general with  $< 0.5$  kpc. These systems have stellar masses  $M_* \sim 10^{9.5} M_\odot$  with our  $z \sim 11.5$  candidate a dwarf galaxy with a stellar mass  $M_* \sim 10^{7.9} M_\odot$ . These candidate ultra high-redshift galaxies are excellent targets for future NIRSpec observations to understand better their physical nature.

**Key words:** galaxies: evolution – galaxies: formation – galaxies: high-redshift

## 1 INTRODUCTION

Following the successful launch of the *James Webb Space Telescope* (JWST) in December of 2021 and the beginning of full scientific operations in July 2022, we have now arrived in a new epoch of extragalactic astronomy. Over the next decade, substantial new datasets probing the near-infrared and mid-infrared wavelength regimes of extragalactic emission across most of the age of the Universe are being made available. As our understanding of not only extragalactic science but also of this new instrumentation improves, it is likely that this field of study will move rapidly as various survey teams generate various observing strategies and analysis pipelines.

A key design goal of the JWST is to push the redshift frontier and search for galaxies that host the first generation of stars when the Universe was less than 5 per cent of its current age. The aim is to tackle questions regarding the formation and evolution of the first galaxies, black holes, and dark matter halos. The history of high-redshift extragalactic astronomy stretches back to the work of Hubble & Humason (1931), while today we know of tens of thousands of galaxies beyond a redshift of 4 (corresponding to 10 per cent of the age of the Universe), and individual galaxies have been found as early

as  $z \sim 10$  (e.g. Bouwens et al. 2011; McLeod et al. 2016; Bouwens et al. 2016; Oesch et al. 2018; Salmon et al. 2018; Morishita et al. 2018; Stefanon et al. 2019; Bowler et al. 2020; Harikane et al. 2022). Yet it remains to be seen how many more galaxies might exist during this epoch of reionization or even earlier, and what their properties are.

JWST provides extensive new capabilities in the near-infrared, enabling us to reach depths many magnitudes deeper than previously possible utilising other near-infrared facilities over the past decade (e.g., HST, the Spitzer Space Telescope and the VISTA telescope). Such an increased depth allows for the Lyman-break and wider rest-frame ultraviolet SED of galaxies with redshifts greater than  $z > 9$  to be probed, providing insight into not only these system’s redshifts but also their stellar mass and star formation rates.

The first releases of data from JWST on the 12th and 13th of July 2022 included the deep data from the RELICS cluster SMACS J0723.3-732 (SMACS 0723, Coe et al. 2019; Ferreira et al. 2022). We examine 8.7 square arcminutes of this cluster’s outer area, with most of this within the second NIRCcam module, to very deep depths (up to  $5\sigma$  AB magnitude 28.9) in the near-infrared. This is thus an ideal initial dataset with which to conduct a search for very high redshift galaxies. Because the depth in SMACS 0723 is comparable or deeper than other early release targets, these data can be used to determine

\* E-mail: nathan.adams@manchester.ac.uk

some of the early demographics of distant galaxies. Furthermore, we are able to make some of the first comparisons with theory (Dayal et al. 2022).

In this paper we present the initial results of our search for  $z > 9$  galaxies within the SMACS 0723 field. We explain our methodology, our completeness calculations, and the basic properties of the galaxies we discovered. We also describe in detail our methodology and how we are able to determine with some certainty that these systems are at high redshift based on their photometric redshift, colours, and properties of their SEDs. To ultimately understand the role of galaxies in the early universe including at the epoch of reionization will require that we build up large samples at these redshifts. Studies such as these are the first step in this process with JWST, which will ultimately address fundamental questions about how reionization occurred and when and how the first galaxies assembled.

The structure of this paper is as follows. In Section 2, we describe the SMACS 0723 observational programme, focussing on the parallel NIRCam observation which we have reprocessed, as well as the data products derived from this new data set. In Section 3 we describe the selection procedure undertaken to define a robust sample of galaxies with redshifts greater than  $z > 9$ . We present an initial analysis of the completion using our procedures and describing the properties of the galaxies we have found. We present a summary of our findings in 4. Throughout this work, we assume a standard cosmology with  $H_0 = 70 \text{ km s}^{-1} \text{ Mpc}^{-1}$ ,  $\Omega_M = 0.3$  and  $\Omega_\Lambda = 0.7$  to allow for ease of comparison with other observational studies. All magnitudes listed follow the AB magnitude system (Oke 1974; Oke & Gunn 1983).

## 2 DATA REDUCTION AND PRODUCTS

The data we use for this analysis originates from the Early Release Observations of SMACS 0723 and include observations taken with the *Near Infrared Camera* (NIRCam; Rieke et al. 2005, 2008, 2015). The images were obtained on June 06, 2022 (PI: Pontoppidan; Program ID 2736) in the F090W, F150W, and F200W short-wavelength (SW) bands, and F356W, F277W, and F444W long-wavelength (LW) bands. The total integration time for this target is 12.5 hr. Figure 1 shows the combined colour image of the second NIRCam module which was not centred on SMACS 0723 which we created from our own reduction.

We reprocess all of the uncalibrated lower-level JWST data products for this field following our modified version of the JWST official pipeline. This is similar process used in Ferreira et al. (2022) but with minor changed and can be summarised as follows: (1) We use version 1.5.2 of the pipeline as opposed to version 1.5.3, which was the most up-to-date version at the time of writing. This is because version 1.5.3 has a significant bug in the background subtraction step that leads to sub-optimal performance.<sup>1</sup> (2) We apply the 1/f noise correction derived by Chris Willott on the resulting level 2 data of the jwst pipeline<sup>2</sup>. (3) We extract the sky subtraction step from stage 3 of the pipeline and run it independently on each NIRCam frame, allowing for quicker assessment of the background subtraction performance and fine-tuning. (4) After Stage 3 of the pipeline, we align the final science images onto a GAIA-derived WCS using *tweakreg*, part of the DrizzlePac python package<sup>3</sup>. We then pixel-match the images with the use of *astropy reproject*<sup>4</sup>. The final resolution of

**Table 1.** A list of the primary parameters used in the running of SExtractor on our imaging.

Parameter	Value
DETECT_MINAREA	9
DETECT_THRESH	1.8
DEBLEND_NTHRESH	32
DEBLEND_MINCOUNT	0.005
BACK_SIZE	64
BACK_FILTERSIZE	3
BACKPHOTO_TYPE	LOCAL
BACKPHOTO_THICK	24

the drizzled images is 0.03 arcseconds/pixel. There is rapid development in the above procedure, and so we anticipate future studies to continue to make adjustments to the JWST pipeline.

Based on the exposure times of the observations conducted of the SMACS 0723 cluster, an initial estimate of the depths that can be achieved in an aperture was obtained through the use of the JWST exposure time calculator. Based on a 0.32 arcsecond circular diameter aperture, the expected depths are F090W = 28.55, F150W = 28.90, F200W = 29.10, F277W = 29.15, F356W = 29.15, and F444W = 28.85. Confirming the data reaches these depths, however, is a challenge. Specifically with this field, there is the lens itself, taking up close to 50 per cent of the usable area with a high density of sources and intra-cluster light. Additionally, there is a large number of very bright stars (GAIA  $m_g < 18.5$ ) inside and on the periphery of the field, creating crisscrossing diffraction spikes that span over a significant portion of the images (much further than can be initially seen from Figure 1). On top of this, there is also the present uncertainty in the behaviour of the telescope’s instruments and its reduction pipeline.

Of particular concern is the handling of flat-fielding, background subtraction, and so-called 1/f noise. We have trialled multiple proposed methodologies for dealing with the above, with mixed results. Imperfections, such as faint vertical/horizontal banding or gradients across the image, have a negative influence on commonly used methodologies to calculate the  $5\sigma$  depth of the image in each photometric band. This includes placing empty circular apertures into the images or using a source subtracted map to examine the RMS of majority sky pixels. We used both of these methods on our images with masking implemented using the segmentation maps, which we derive later on in this paper, as well as manual masking of prominent diffraction spikes and 1/f banding that is still visible after our attempts to correct them.

Examining the RMS of sky pixels in our unmasked areas, we estimate depths of F090W = 28.2, F150W = 28.2, F200W = 28.4, F277W = 28.9, F356W = 28.9, and F444W = 28.45 in 0.32 arcsecond diameter circular apertures. Compared to the theoretical estimates, it is clear that the pipeline has performed better during the processing of the red module of NIRCam than the blue module. All considered, it is likely that the bluest bands can be pushed deeper with a refined reduction pipeline in the future.

### 2.1 Source Photometry and Cataloguing

With the final mosaics of the field completed, we carry out source identification and extraction. For this process, we use the code SExtractor (Bertin & Arnouts 1996). We generate multiple different source catalogues for use in calculating the total source counts in each photometric band as a sanity check on our reduction process, with typical detection parameters shown in Table 1. For the purpose

<sup>1</sup> <https://github.com/spacetelescope/jwst/issues/6920>

<sup>2</sup> <https://github.com/chriswillott/jwst>

<sup>3</sup> <https://github.com/spacetelescope/drizzlepac>

<sup>4</sup> <https://reproject.readthedocs.io/en/stable/>



**Figure 1.** A colour composite based on our own reduction of NIRCcam imaging of the SMACS 0723 parallel field. This composite utilises data acquired in 6 bands: F090W, F150W, F200W, F277W, F356W, and F444W, each band being assigned a different colour, sequentially from blue to red. F090W and F150W were mapped to blue hues, F200W and F277W to green, and F356W and F444W to orange and red respectively.

of this paper, we generate a catalogue which applies forced photometry on the images, using the F200W band as the selection band. This is specifically optimized for the detection of high-redshift galaxies at  $9 < z < 12$ . Output catalogues include basic information about source positions and sizes along with forced aperture photometry. This aperture photometry is calculated within 0.32 arcsecond diameter circular apertures and is corrected with an aperture correction derived from simulated WebbPSF point spread functions for each band used. This diameter was chosen to enclose the central/brightest 70 – 80 per cent of the flux of a point source, enabling us to use the highest SNR pixels to calculate galaxy colours while avoiding a reliance on a strong aperture correction.

### 3 A ROBUST SAMPLE OF ULTRA-HIGH REDSHIFT SOURCES

With the imaging and cataloguing completed, we carried out a search for high-redshift sources embedded deep within the epoch of reionisation (at  $z > 9$ ). For this first search, we approach this problem in a conservative manner, employing stringent cuts to ensure a pure and robust sample of candidates. It is for this reason that we employ a magnitude cut of 28 in the F200W band within a 0.32 arcsec diameter aperture. This equates to  $7.5\sigma$  based on our initial depth calculations. Such a bright magnitude is used to ensure that Lyman-breaks are correctly identified as such and are not actually Balmer-breaks at lower redshift. Since the F090W filter is of depth 28.2 (providing  $2\sigma$  limits of 29.2), if we were to push the limits of the field with a deeper F200W selection, the F090W filter will not be deep enough for a non-detection to rule out a deep Balmer-break or smoother SED indicative

of a lower- $z$  galaxy. Additionally, the SMACS 0723 observations unfortunately lacks the F115W filter that is available with NIRCcam and is being used by nearly every other deep field at present, potentially reducing the performance of photometric redshifts and colour cuts. As our understanding of both the instrumentation aboard JWST and the SEDs of ultra-high redshift galaxies improve, it is likely that we will be able to make full use of the depths available in the near future, but for now there is some risk of faint/low-mass  $z \sim 2 - 3$  interlopers falling into the selection criteria if stringent cuts are not made. However, we are confident that we have managed to remove most of this contamination.

#### 3.1 Spectral Energy Distribution Modelling and Photometric redshifts

Our photometric redshifts employ the use of multiple different commonly used codes, each of which makes use of different statistical methodologies. We use LePhare (minimising chi square) with checks from other codes to insure a consistency.

Our first round of SED fitting utilises LePhare (Arnouts et al. 1999; Ilbert et al. 2006) to conduct an initial measurement of the photometric redshift of the sources in our catalogue with a greater than  $10\sigma$  detection in the selection band of the catalogue. We set this code up to fit templates from Bruzual & Charlot (2003) with the Chabrier et al. (2000) IMF, using exponential star formation histories with 10 characteristic timescales between  $0.01 < \tau < 13$  Gyr, and 57 different ages between 0 and 13 Gyr. The redshift range allowed is  $0 < z < 15$ , and we apply dust attenuation following Calzetti et al. (2000). The treatment for the IGM attenuation derived in Madau

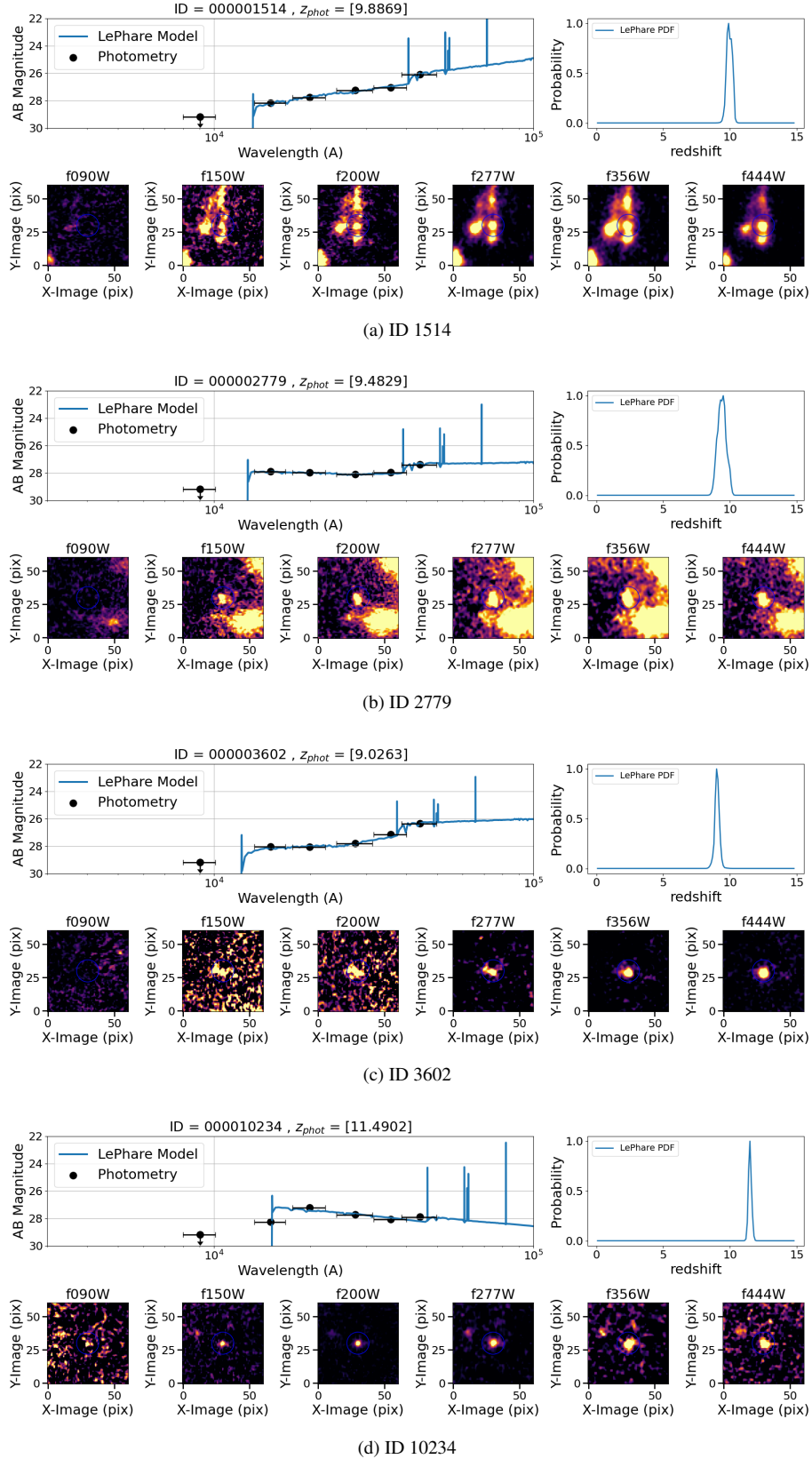


**Figure 2.** Here we present the SEDs for the 4 new candidate  $z > 9$  galaxies identified in this study, showing the photometry in the different JWST bands as observed with NIRCam. Overplotted on each panel is the best-fit LePhare model for the SED for these galaxies from which the photometric redshifts are derived. We also show the PDF of the photometric redshift distribution, and in the bottom panel the images in our six bands. The pixel scale of these images is 0.03 arcseconds per pixel.



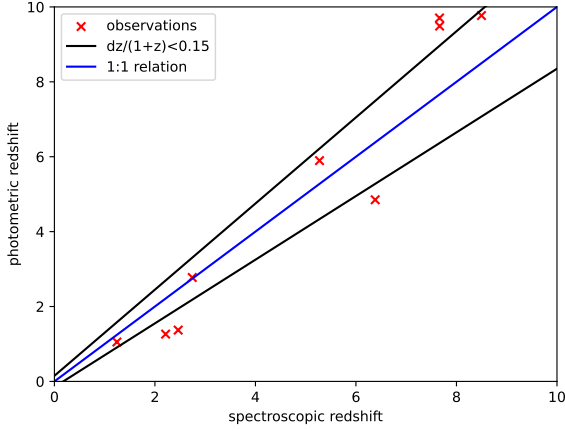


**Figure 3.** Initial diagnostics for the performance of the LePhare spectroscopic redshifts. We compare our photometric redshifts with spectroscopic redshifts for a NIRSpc sample measured by Carnall et al. (2022). As can be seen, we find a generally good agreement between these spectroscopic redshifts and our photometric ones, with some scatter.

(1995) is also applied. The photometry is given a minimum error of 5 per cent.

To validate the photometric redshifts, we compare to some of the initial NIRSpc spectroscopic analysis of Carnall et al. (2022). We use the 10 spectroscopic redshifts provided by this study, 5 for lower redshift sources and 5 for higher redshift sources. We find that 9 of these have a cross-match to our F200W selected catalogue. We present the comparison in Figure 3. We find that the agreement between our photo- $z$ s and these spec- $z$ s is reasonably good, considering the wavelength range available, number of bands in use, and, critically, the lack of the F115W band. A total of 4/9 objects satisfy the typical photometric redshift definition of not being an outlier (Normalised Mean Absolute Deviation (NMAD)  $|\delta z|/(1+z) < 0.15$ ). This increases to 7/9 if the tolerance is relaxed to  $|\delta z|/(1+z) < 0.25$ , with the two remaining outliers being those at  $z \sim 2.25$ . All three F090W break objects are correctly identified as being at high redshifts,  $z > 7$ , but our redshift measures are found to be systematically higher in redshift. The cause of this is likely the very high  $H\beta$  and [OIII] equivalent widths determined in the spectrophotometric analysis conducted in Carnall et al. (2022). This would inflate the F444W measurement and shift a photometric redshift higher if the lines strengths in the templates are not as high as in reality. In either case, our procedure has shown to be effective at identifying F090W break galaxies, though the precise final redshifts are tentative until spectroscopy can be obtained.

All sources meeting an initial cut of  $z > 9$  and  $m_{F200W} < 28$  are visually inspected to remove objects that are close to the image edge or that are clearly under the influence of artefacts (such as diffraction spikes). This process leaves us with a total of 15 candidates out of the 5350 that are brighter than magnitude 28 in F200W. To ensure the sample is as pure as possible, we require that the majority of the probability density be above  $z = 9$ . This removed 8 sources which had strong secondary peaks at  $2 < z < 3$  and were at risk of a Lyman/Balmer-break confusion. Of the 7 remaining, 3 had spectroscopic redshifts previously discussed, leaving us with a final sample of 4 new sources with photometric redshifts greater than 9. The final SEDs of these four new sources are presented in Figure 2.

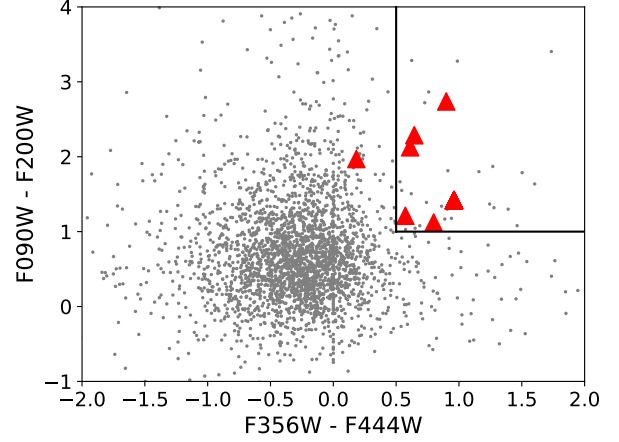


**Figure 4.** A colour-colour diagram spanning the Lyman-break (F090W-F200W) and Balmer-break F356W-F444W of our high redshift targets and the wider catalogue of objects in the SMACS0723 field. As all of our targets are drop-outs in F090W, the red triangles represent a  $2\sigma$  lower limit pointing upwards in the F090W-F200W colour space. The one object outside of the upper right quadrant is our  $z = 11.5$  candidate.

### 3.1.1 Locations of the targets in colour space

As a sanity check of our targets, we examine their location in colour space. In particular, we examine the colour space spanning the Lyman and Balmer-breaks of these objects. The colour-colour diagram comprising these breaks is shown in Figure 4 for both our sample and the catalogue as a whole. The upper right quadrant indicates objects with sharp breaks or strong emission lines in SED where Lyman and Balmer-breaks (or the  $H\beta$  and [OIII] lines) would be expected for such high- $z$  targets. We plot on this limits of a break strength of 1.0 mags in the bands spanning the Lyman-break as well as 0.5 mags in the Balmer-break.

Beyond redshifts of 11, however, the Balmer-break has shifted redwards enough such that it is beginning to exit the F444W band. It is thus not surprising that the target with the weakest Balmer-break is our candidate at  $z \sim 11.5$ . The redshift for this object is justified on the basis of a 0.4 magnitude drop between the F150W and F200W bands combined with the non-detection in F090W. Objects within this colour region, but not reaching our final sample, have significant contamination, are too faint for our limits, or have a photo- $z > 9$  with no secondary peak to lower redshifts.

### 3.2 Completeness Analysis

We carry out completeness tests on our data using a simple simulation to extract fake sources that are inserted into the images. To conduct this, we insert galaxies with a Sérsic index of 1 and  $M_{UV}$  luminosities ranging from -19 to -24 into the F200W image used for our selection. Half light radii of the fake sources are of different sizes, which are designed to match the theoretical predicted sizes of distant galaxies from BlueTides (Feng et al. 2016; Wilkins et al. 2017; Marshall et al. 2022). The simulation was carried out by sweeping the magnitude range in 0.2 mag intervals, placing 1000 galaxies in the SMACS 0723 parallel field for each interval, and then running SExtractor in the same way on this field as we did for our original detection. A size-luminosity relation of  $r \propto L^{0.5}$  was assumed throughout (Grazian et al. 2012), with a reference radius of 800 pc at  $M_{UV} = -21$  and assuming source redshifts of 10.5, the middle of the range considered

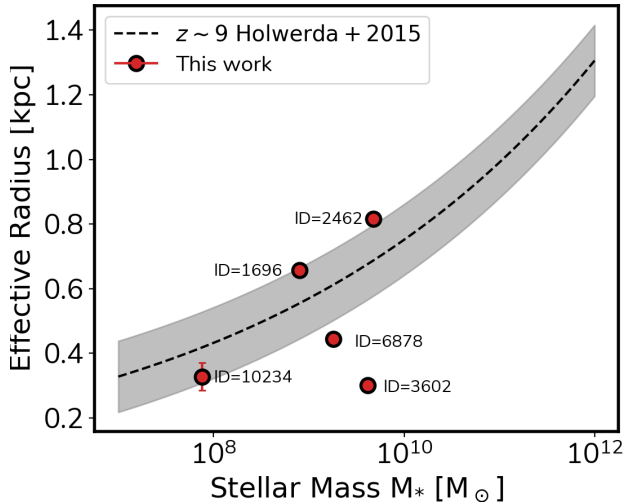


**Figure 5.** Effective radius vs stellar mass. Red outline points are the sources reported with structural measurements, dashed black line best fit to size–stellar mass relation from [Holwerda et al. \(2015\)](#).

in this study. This allows us to determine how well we can retrieve galaxies of different brightnesses at the redshifts of our objects.

In summary, we find we are able to recover more than 50% of the simulated galaxies at  $z = 10.5$  down to a luminosity limit of  $M_{UV} = -22$ , assuming this size limit. This increases for smaller sized galaxies. This recovery fraction also increases to 90% for sources with  $M_{UV} = -23$ .

### 3.3 Galaxy Structure

For the purposes of this work, we limit our structural analysis to the light profiles of our sources through single-component Sérsic profiles in the F444W band as measured by Morfometryka ([Ferrari et al. 2015](#)). We include in this analysis the sources verified as being at  $z > 7$  from [Carnall et al. \(2022\)](#). As input into this part we use 64x64 pixels stamps as well as a PSF generated with WEBBPSF. This code measures the luminosity growth curve through aperture photometry in a segmented region based on the Petrosian radius. A 1D Sérsic fit is performed on the luminosity profile, which in turn is used as inputs to a 2D Sérsic fit done with the galaxy and the PSF images.

We list the sizes in terms of the effective radius ( $R_e$ ) in kpc as well as the Sérsic index ( $n$ ), which defines the steepness of the light profile. These values are listed in Table 3. Examples of the fitting procedure, the models, and residuals are shown in Figure 8.

Overall, the sources exhibit structures resembling light profiles of disk-like systems, consistent with exponential light profiles. The exception is ID 3602 which displays a concentrated core even within the uncertainties. We also find that the galaxies in our sample are very small. For the most part we find that the effective radii of our systems is  $< 0.5$  kpc, with all systems  $< 1$  kpc. Figure 5 shows the location of the objects we examine with reference to a previously published  $z = 9$  stellar mass vs. effective radius diagram. Whilst some of our objects are consistent with this relation, three of them appear to be smaller than their stellar mass would imply.

### 3.4 An unusual red structure in the secondary SMACS0723 observation

Among our final list of high- $z$  candidates is ID 1514 which is located in the NIRCam module that is not centered on the SMACS0723 cluster. In our inspection of our candidates, we find that ID 1514 ( $RA = 110.61465$ ,  $DEC = -73.4774$ ) is potentially a part of a wider structure located at high redshift. ID 1514 is the bright, compact centre component of the circled system shown in Figure 6. Within close physical proximity, the target has three neighbouring objects with very red colours. The object immediately below it has a photometric redshift that is similar to ID 1514 at  $z_{\text{phot}} = 9.3 \pm 0.3$ , the object immediately above is also a F090W dropout but was provided a redshift of  $8.6 \pm 0.6$  by our template fitting procedure.

The final object, located to the left, has a slight detection in F090W and a redshift of  $6.15 \pm 0.4$ . The exact nature of this structure is presently unknown, but since the majority of this structure drops out in the F090W band, it is warranting of a mention and further follow-up investigation is planned for the near future.

### 3.5 Comparisons to Predictions from Theory

Although we have just started to probe this epoch in the universe’s history, we can make basic predictions to theory in terms of how many galaxies we would expect at these magnitudes and redshifts. We carry out a preliminary comparison to a number of models as shown in Fig. 7. These include phenomenological models ([Mason et al. 2015](#)), semi-analytic models including Delphi ([Dayal et al. 2014, 2022](#)) and (the Santa Cruz model; [Yung et al. 2019](#)) and hydrodynamical simulations including Bluetides ([Feng et al. 2016; Wilkins et al. 2017](#)) and FLARES ([Lovell et al. 2021; Vijayan et al. 2021; Wilkins et al. 2022](#)). All of these models are shown in Fig. 7 in terms of the cumulative number of systems at  $z > 9$ . What can be seen in all models, and in our data, is that we have fewer systems at higher redshifts given our magnitude limit.

For our magnitude limit of 28.6 in the NIRCAM F277W filter, these models predict 2–10 objects at  $z \gtrsim 9$  which is in agreement with the 4 sources presented in this work. As expected, for this magnitude limit, the numbers fall off with increasing redshift, with anywhere between 0.03 and 0.5 such objects expected at  $z \gtrsim 11.5$ ; this is somewhat lower than the 1 such source in this work. Finally, we note that the highest amplitudes of the number counts are predicted by DELPHI and FLARES. The DELPHI model being an upper limit is perhaps not surprising since it has been base-lined against the most recent dust estimates from the REBELS (Reionization Era Bright Emission Line Survey) ALMA large program ([Bouwens et al. 2022](#)). As shown in previous works ([Dayal et al. 2022](#)), a number of REBELS sources show exceedingly high dust-to-stellar mass ratios leading to a significant attenuation of the UV light; this requires high SFR to be able to reproduce high- $z$  observables. While our number counts are very small and still have large counting and cosmic variance uncertainties, this attempt shows that we are now able to compare at these higher redshifts where differences between models can be observed and tested.

## 4 CONCLUSIONS

We have carried out one of the first analyses of the very early universe using the early release observations (ERO) data from JWST near the cluster field SMACS 0723. Within this field, we identify 4 new  $z > 9$  galaxy candidates based on photometric redshifts and colour

**Table 2.** A complete list of the coordinates and photometric information for our candidate high-redshift sources. In the first column, we provide the identifying number within our catalogues, the second and third columns detail the right ascension and declination coordinates of the candidate, column 4 provides the redshift as measured in our template fitting process. Column 5 contains a spectroscopic redshift if one was previously available. Columns 6-11 detail the measured aperture-corrected photometry within 0.32 arcsecond diameter circles in the NIRCcam imaging. Table 3 lists the physical and morphological properties of these galaxies.

ID	R.A.	Dec.	ZPhot	ZSpec	F090W	F150W	F200W	F277W	F356W	F444W
1514	110.61465	-73.4774	$9.89^{+0.37}_{-0.24}$	–	> 29.2	$28.18 \pm 0.08$	$27.77 \pm 0.05$	$27.25 \pm 0.05$	$27.06 \pm 0.05$	$26.10 \pm 0.05$
1696	110.83401	-73.43453	$9.70^{+0.33}_{-0.24}$	7.663	> 29.2	$26.81 \pm 0.05$	$26.91 \pm 0.05$	$26.74 \pm 0.05$	$26.69 \pm 0.05$	$26.04 \pm 0.05$
2462	110.84460	-73.43507	$9.49^{+0.25}_{-0.24}$	7.665	> 29.2	$26.49 \pm 0.05$	$26.46 \pm 0.05$	$25.98 \pm 0.05$	$25.73 \pm 0.05$	$24.83 \pm 0.05$
2779	110.64606	-73.47585	$9.48^{+0.28}_{-0.24}$	–	> 29.2	$27.91 \pm 0.06$	$27.98 \pm 0.06$	$28.11 \pm 0.05$	$27.98 \pm 0.05$	$27.40 \pm 0.05$
3602	110.86129	-73.43627	$9.03^{+0.20}_{-0.24}$	–	> 29.2	$28.06 \pm 0.09$	$27.98 \pm 0.06$	$27.81 \pm 0.05$	$27.16 \pm 0.05$	$26.10 \pm 0.05$
6878	110.85936	-73.44916	$9.77^{+0.25}_{-0.27}$	8.498	> 29.2	$27.11 \pm 0.05$	$27.07 \pm 0.05$	$26.76 \pm 0.05$	$26.72 \pm 0.05$	$26.11 \pm 0.05$
10234	110.66501	-73.50174	$11.49^{+0.11}_{-0.10}$	–	> 29.2	$28.27 \pm 0.11$	$27.23 \pm 0.05$	$27.73 \pm 0.05$	$28.08 \pm 0.05$	$27.90 \pm 0.05$

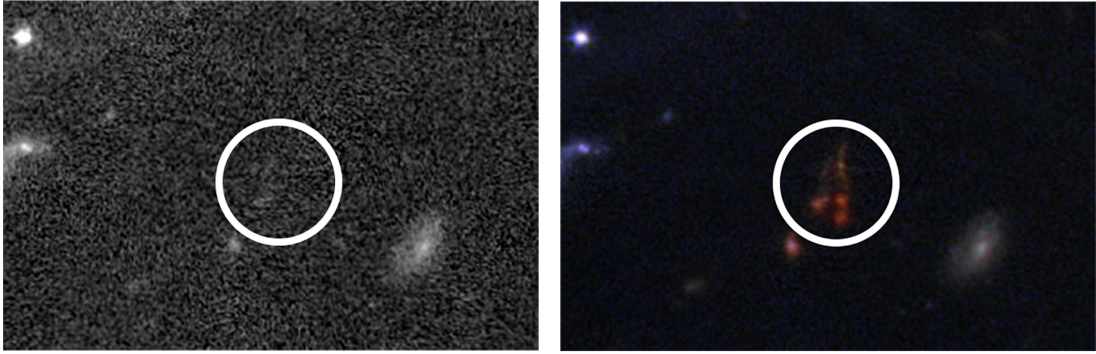


**Figure 6.** A zoom into the colour composite presented in Figure 1. The circled object is a large F090W drop out structure composed primarily of 4 closely neighbouring sources in the ‘blank’ part of the SMACS field. The right panel shows the colour image created from six filter bands (as described in the caption to Figure 1, while the left panel shows the F190W image, in which the object(s) drop out.

**Table 3.** The results of the structural fitting process on our list of candidates. Here we display the best fitting photometric redshift from LePhare, unless a spectroscopic redshift is available. The stellar mass is obtained by fixing the redshift to the best redshift and running through LePhare. Alongside we show the size and Sérsic index for each galaxy in which a clean fit was possible. Errors on the stellar masses are typically  $\pm 0.2$  for the stellar populations models we use.

ID	z	$\sim \log(M_*)$	n	$R_e$ [kpc]
1514	9.89	10.2	–	–
1696	7.663	8.9	$1.28 \pm 0.05$	$0.65 \pm 0.01$
2462	7.665	9.7	$0.74 \pm 0.2$	$0.81 \pm 0.01$
2779	9.48	9.0	–	–
3602	9.03	9.6	$3.05 \pm 0.44$	$0.3 \pm 0.02$
6878	8.498	9.3	$1.94 \pm 0.15$	$0.44 \pm 0.01$
10234	11.49	7.9	$2.11 \pm 0.98$	$0.32 \pm 0.04$

cuts, with one object at  $z = 11.5$  and another object potentially a part of a more complex, multi-component system. The number of galaxies broadly match theoretical predictions for the volume and depth probed by this ERO data. The region occupied by the foreground galaxy cluster has also not been fully analysed. Meaning there is further opportunity to find extremely high redshift galaxies that have been strongly lensed in this field.

We find that these systems are robust candidates due to the fact that we find both a Lyman-break and one of a Balmer-break or strong  $H\beta$  and  $O[III]$  emission; are present within the SEDs of the spectrum of these galaxies. Follow up spectroscopy will be required to both confirm the redshifts of these galaxies and probe the stellar

population. The possible degeneracy in Balmer-breaks and extreme line emission mean that understanding if the stellar population is extremely young or old for the time is difficult to achieve with purely photometric means at this time.

We also find that these early galaxies can be well fit by simple parametric fitting and have Sérsic indices which are around  $n = 1$ , but with some systems having higher indices, a possible indication of an early structural evolution for galaxies.

Our findings point the way towards the future when large samples of high- $z$  galaxies, such as these and at even higher redshifts, become available from larger area and deeper JWST data that is on the horizon. Using these samples we will be able to reconstruct the history of reionization and the earliest formation of galaxies.

## ACKNOWLEDGEMENTS

We thank Anthony Holloway, Sotirios Sanidas and Phil Perry for critical and timely help with computer infrastructure that made this work possible. We acknowledge support from the ERC Advanced Investigator Grant EPOCHS (788113), as well as a studentship from STFC. This work is based on observations made with the NASA/ESA Hubble Space Telescope (HST) and NASA/ESA/CSA James Webb Space Telescope (JWST) obtained from the Mikulski Archive for Space Telescopes (MAST) at the Space Telescope Science Institute (STScI), which is operated by the Association of Universities for Research in Astronomy, Inc., under NASA contract NAS 5-03127 for JWST, and NAS 5-26555 for HST. These observations are associated with program 14096 for HST, and 2736 for JWST. LF

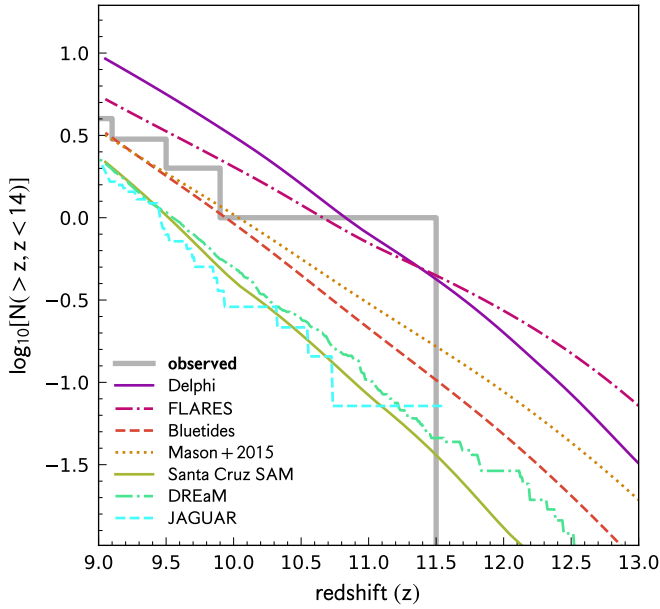


**Figure 7.** Comparison between different models for how many high redshift galaxies at  $z > 9$  we should detect within our probed area of SMACS 0723. Included here are the predictions from (Mason et al. 2015), the semi-analytic model Delphi (Dayal et al. 2014, 2022) and (the Santa Cruz model Yung et al. 2016; Wilkins et al. 2017) and FLARES (Lovell et al. 2021; Vijayan et al. 2021; Wilkins et al. 2022). Dayal et al. (2020).

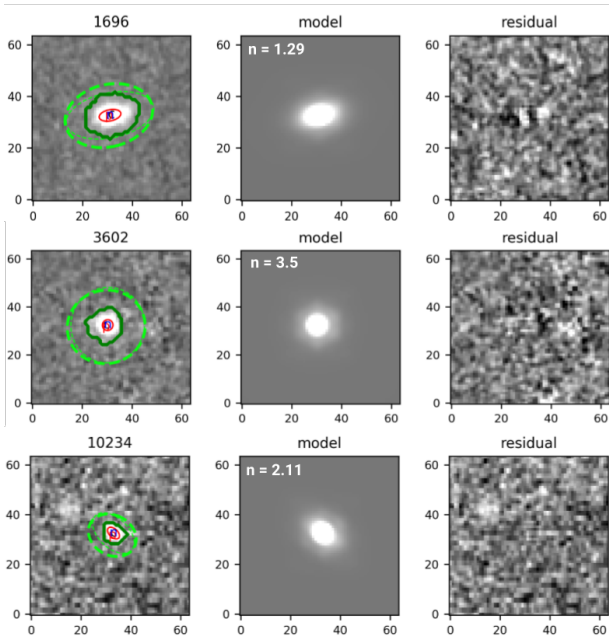


**Figure 8.** Sérsic profile fits for 3 of our high- $z$  candidates. Left panels show the source along with its Petrosian region in dashed light green, the 2D Sérsic model is shown in the central panel, together with its Sérsic index ( $n$ ), right panel displays the residuals after source subtraction. Profiles are fitted with the MORFOMETRYKA code, as in Ferreira et al. (2022).

acknowledges financial support from Coordenação de Aperfeiçoamento de Pessoal de Nível Superior - Brazil (CAPES) in the form of a PhD studentship. PD acknowledges support from the NWO grant 016.VIDI.189.162 (“ODIN”) and the European Commission’s and University of Groningen’s CO-FUND Rosalind Franklin program.

## REFERENCES

- Arnouts S., Cristiani S., Moscardini L., Matarrese S., Lucchin F., Fontana A., Giallongo E., 1999, *MNRAS*, **310**, 540
- Bertin E., Arnouts S., 1996, *A&AS*, **117**, 393
- Bouwens R. J., et al., 2011, *Nature*, **469**, 504
- Bouwens R. J., et al., 2016, *ApJ*, **833**, 72
- Bouwens R. J., et al., 2022, *ApJ*, **931**, 160
- Bowler R. A. A., Jarvis M. J., Dunlop J. S., McLure R. J., McLeod D. J., Adams N. J., Milvang-Jensen B., McCracken H. J., 2020, *MNRAS*, **493**, 2059
- Bruzual G., Charlot S., 2003, *MNRAS*, **344**, 1000
- Calzetti D., Armus L., Bohlin R. C., Kinney A. L., Koornneef J., Storchi-Bergmann T., 2000, *ApJ*, **533**, 682
- Carnall A. C., et al., 2022, arXiv e-prints, p. [arXiv:2207.08778](https://arxiv.org/abs/2207.08778)
- Chabrier G., Baraffe I., Allard F., Hauschildt P., 2000, *ApJ*, **542**, 464
- Coe D., et al., 2019, *ApJ*, **884**, 85
- Dayal P., Ferrara A., Dunlop J. S., Pacucci F., 2014, *MNRAS*, **445**, 2545
- Dayal P., et al., 2020, *MNRAS*, **495**, 3065
- Dayal P., et al., 2022, *MNRAS*, **512**, 989
- Feng Y., Di-Matteo T., Croft R. A., Bird S., Battaglia N., Wilkins S., 2016, *MNRAS*, **455**, 2778
- Ferrari F., de Carvalho R. R., Trevisan M., 2015, *ApJ*, **814**, 55
- Ferreira L., et al., 2022, arXiv e-prints, p. [arXiv:2207.09428](https://arxiv.org/abs/2207.09428)
- Grazian A., et al., 2012, *A&A*, **547**, A51
- Harikane Y., et al., 2022, *ApJ*, **929**, 1
- Holwerda B. W., Bouwens R., Oesch P., Smit R., Illingworth G., Labbé I., 2015, *ApJ*, **808**, 6
- Hubble E., Humason M. L., 1931, *ApJ*, **74**, 43
- Ilbert O., et al., 2006, *A&A*, **457**, 841
- Lovell C. C., Vijayan A. P., Thomas P. A., Wilkins S. M., Barnes D. J., Irodoutou D., Roper W., 2021, *MNRAS*, **500**, 2127
- Madau P., 1995, *ApJ*, **441**, 18
- Marshall M. A., et al., 2022, arXiv e-prints, p. [arXiv:2206.08941](https://arxiv.org/abs/2206.08941)
- Mason C. A., et al., 2015, *ApJ*, **805**, 79
- McLeod D. J., McLure R. J., Dunlop J. S., 2016, *MNRAS*, **459**, 3812
- Morishita T., et al., 2018, *ApJ*, **867**, 150
- Oesch P. A., Bouwens R. J., Illingworth G. D., Labbé I., Stefanon M., 2018, *ApJ*, **855**, 105
- Oke J. B., 1974, *ApJS*, **27**, 21
- Oke J. B., Gunn J. E., 1983, *ApJ*, **266**, 713
- Rieke M., Kelly D., Horner S., NIRCeam Team 2005, in American Astronomical Society Meeting Abstracts. p. 115.09
- Rieke M. J., et al., 2008, in American Astronomical Society Meeting Abstracts #212. p. 79.01
- Rieke G. H., et al., 2015, *PASP*, **127**, 584
- Salmon B., et al., 2018, *ApJ*, **864**, L22
- Stefanon M., et al., 2019, *ApJ*, **883**, 99
- Vijayan A. P., Lovell C. C., Wilkins S. M., Thomas P. A., Barnes D. J., Irodoutou D., Kuusisto J., Roper W. J., 2021, *MNRAS*, **501**, 3289
- Wilkins S. M., Feng Y., Di Matteo T., Croft R., Lovell C. C., Waters D., 2017, *MNRAS*, **469**, 2517
- Wilkins S. M., et al., 2022, arXiv e-prints, p. [arXiv:2204.09431](https://arxiv.org/abs/2204.09431)
- Yung L. Y. A., Somerville R. S., Popping G., Finkelstein S. L., Ferguson H. C., Davé R., 2019, *MNRAS*, **490**, 2855

This paper has been typeset from a  $\text{\LaTeX}$  file prepared by the author.